ACI MATERIALS JOURNAL TECHNICAL PAPER

Title no. 110-M33

Micromechanics of High-Strength, High-Ductility Concrete

by Ravi Ranade, Victor C. Li, Michael D. Stults, Todd S. Rushing, Jason Roth, and William F. Heard

This paper reports the microscale investigation of a new fiber-reinforced cementitious composite, high-strength, high-ductility concrete (HSHDC), which possesses a rare combination of very high compressive strength (166 MPa [24.1 ksi]) and very high tensile ductility (3.4% strain capacity). The investigation involved experimental determination of fiber/matrix interaction properties using single-fiber pullout tests. A new mechanism of inclination-dependent hardening in fiber pullout—unique for a high-strength cementitious matrix—is discovered. The existing fiber-pullout analytical model for strain-hardening cementitious composites (SHCCs) is modified to incorporate the new mechanism. The modeled fiber-pullout behavior is used in a scale-linking model to compute the crack bridging (σ-δ) relation of HSHDC, which is also empirically verified through single-crack tests. The σ-δ relation of HSHDC satisfies the micromechanics-based necessary strength and energy conditions of steady-state flat crack propagation that prevent localized fracture. The microscale investigation of HSHDC in this research thus demonstrates the rational basis for its design combining both high compressive strength and high tensile ductility.

Keywords: high-ductility concrete; high-performance cementitious composite; high-strength concrete; micromechanics.

INTRODUCTION

The modern-day frontiers of concrete can be defined by material characteristics—high compressive strength and high tensile ductility. Materials such as very-high-strength concrete (VHSC) and ultra-high-performance concretes (UHPCs) exhibit compressive strengths in excess of 200 MPa (29 ksi), reaching up to 800 MPa (116 ksi).[1,2] On the other hand, strain-hardening cementitious composites (SHCCs) exhibit very high tensile ductility with strain capacities of 3 to 6% (20 to 40 times that of VHSC/UHPC).[3-6] As a result of their contrasting material properties, VHSC/UHPC and SHCC have different structural applications—VHSC/UHPC are often used to achieve size efficiency in structural members, whereas SHCCs are used to achieve durability and ductile structural performance.

The authors of this paper have recently succeeded in designing a high-strength, high-ductility concrete (HSHDC) that combines very high compressive strength (166 MPa [24.1 ksi]) and very high tensile ductility with 3.4% average tensile strain capacity under direct tension loading (Fig. 1).[7] The unique performance of HSHDC is achieved through deliberate selection of fiber, matrix, and their interface, guided by the micromechanics-based design principles developed by Li and coworkers[8-10] for engineered cementitious composites (ECC—a type of SHCC) while incorporating the VHSC matrix.[11]

The objectives of this paper are: first, to determine the microscale fiber/matrix interaction properties in HSHDC; second, to ascertain whether the existing analytical fiber-pullout model for SHCC completely explains the experimental fiber-pullout behavior of HSHDC (and if not, investigate any new mechanisms); and third, to test whether the fundamental micromechanics-based conditions for strain hardening are satisfied by HSHDC. The achievement of these objectives in this paper generated new knowledge of micromechanical properties and interaction mechanisms of a high-performance fiber (ultra-high-molecular-weight polyethylene [UHMWPE]) with a very-high-strength cementitious matrix, in contrast with the typically used polyvinyl alcohol (PVA) fiber and moderate-strength matrix in SHCC. This study establishes a micromechanics basis for the observed composite tensile strain-hardening behavior of HSHDC, reported in a companion paper[7] (Fig. 1), by investigating microscale fiber/matrix interactions.

The micromechanical investigation procedure followed in this research for achieving the aforementioned objectives is shown schematically in Fig. 2. Single-fiber pullout tests were performed with varying embedment lengths and inclination angles with respect to the loading direction. While the existing debond and pullout models[8] (originally developed for SHCC) were able to explain the observed aligned fiber (inclination angle = 0 degrees) pullout satisfactorily, the increase in pullout load with inclination of fibers (observed in HSHDC in addition to the snubbing effect) could not be captured by these models. A new inclination-dependent hardening mechanism was proposed to explain the observed inclined fiber pullout in HSHDC, which was found to be unique to the high-strength matrixes and beneficial for fiber bridging in HSHDC. The fiber-pullout mathematical model for SHCC was modified accordingly to capture the new mechanism. The fiber/matrix interaction properties and mechanisms thus inferred from the single-fiber pullout test results were used in a statistical scale-linking model[12] to analytically compute the bridging stress-crack opening (σ-δ) relation of HSHDC. This computed σ-δ relation was experimentally verified through single-crack tests using notched rectangular coupon specimens. The σ-δ relation was finally used to check the two necessary conditions of multiple cracking[13] to achieve composite tensile ductility. Details of the micromechanical investigation of HSHDC following the aforementioned procedure are documented in this paper.

RESEARCH SIGNIFICANCE

Increasing compressive strength and tensile ductility of concrete materials simultaneously has been a long-standing design challenge. This paper documents the micromechanical analysis of a new material—HSHDC—which bears a unique combination of high compressive strength and high tensile ductility. Experimentally determined fiber/matrix

ACI Materials Journal, V. 110, No. 4, July-August 2013.
MS No. M-2011-243.R1 received November 27, 2012, and reviewed under Institute publication policies. Pertinent discussion including author's closure, if any, will be published in the May-June 2014 *ACI Materials Journal* if the discussion is received by February 1, 2014.

ACI member **Ravi Ranade** *is a Graduate Student Research Assistant in the Department of Civil and Environmental Engineering at the University of Michigan, Ann Arbor, MI. He received his BS in civil engineering from the Indian Institute of Technology, Mumbai, India, and his MSE in civil engineering (structures) from the University of Michigan. His research interests include the development of advanced cementitious composites for resilient and sustainable infrastructure systems.*

Victor C. Li, *FACI, is the E.B. Wylie Professor in the Civil and Environmental Engineering Department at the University of Michigan. His research interests include the micromechanics and design of ultra-ductile and green cementitious composites, their application to innovative and sustainable infrastructure systems, and integration of materials and structural design.*

ACI member **Michael D. Stults** *is a Structural Designer at Tuan and Robinson Structural Engineers, Inc., San Francisco, CA. He received his BS in physics from Azusa Pacific University, Azusa, CA, and his MSE in civil engineering (structures) from the University of Michigan. His research interests include the design of advanced cementitious composites using recycled materials for achieving a sustainable and resilient infrastructure in developing countries.*

Todd S. Rushing *is a Research Scientist at the U.S. Army Engineer Research and Development Center (ERDC), Vicksburg, MS. He received his BS in chemical engineering from the University of Mississippi, Oxford, MS, and his PhD in polymer science and engineering from the University of Southern Mississippi, Hattiesburg, MS. His research interests include development, processing, and characterization of a variety of cementitious and synthetic materials and composites.*

Jason Roth *is a Research Structural Engineer at ERDC. He received his BS and MS from Mississippi State University, Oktibbeha County, MS, and is a PhD student at the University of California, Los Angeles, CA. His research interests include the development of high-performance materials and structures to resist blast and impact loading for defense applications.*

William F. Heard *is a Research Structural Engineer at ERDC. He received his BS and MS from Mississippi State University and is a current PhD student at Vanderbilt University, Nashville, TN. His research interests include the development and characterization of cementitious composites for blast and impact loading.*

interaction properties in this paper provide physical insights into the microscale interaction of the fiber-matrix-interface in HSHDC. The new knowledge of the fiber/matrix interaction mechanism is expected to be instrumental in the future designs of similar materials with high-strength matrixes. The micromechanical analysis provides a basis for rational design and continued systematic improvement of the mechanical performance of HSHDC.

EXPERIMENTAL INVESTIGATION

Materials and mixture proportions

The mixture proportions and particle sizes of constituents of HSHDC are given in Table 1. UHMWPE (henceforth referred as "PE") fibers (properties in Table 2) are used in HSHDC compared to steel fibers in VHSC. The matrix of HSHDC presented herein is based on the VHSC developed by O'Neil.[11] Modifications to the matrix were made to achieve adequate dispersion of PE fibers and desired fiber/matrix interfacial bond. The sand/cement ratio was decreased in HSHDC to 0.70 as compared to 0.97 in VHSC. In addition, the HRWRA/cementitious material ratio was increased to 1.26% in HSHDC from 0.61% in VHSC. Similar to other high-performance concretes, HSHDC consists of cementitious materials, fine aggregates, fibers, water, and HRWRA; further details about the constituents and material design are presented in Ranade et al.[7,14]

Specimen preparation and testing procedures

Two types of specimens were prepared for mechanical testing in this research: 1) single-fiber pullout specimens;

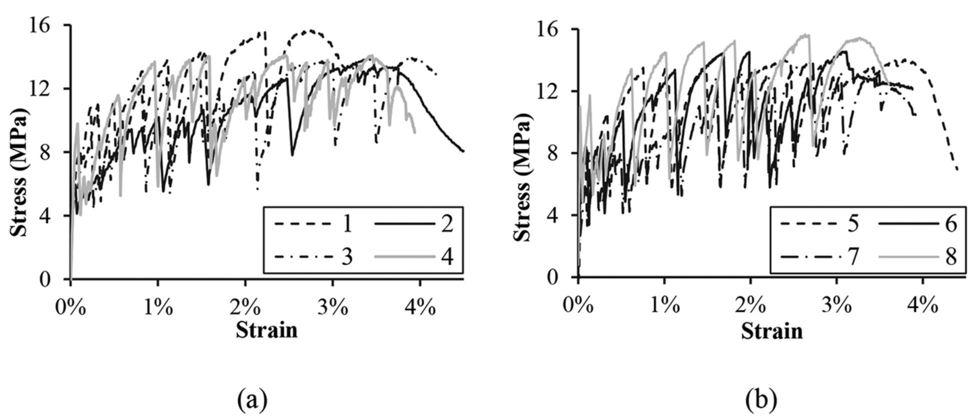

Fig. 1—Direct tension test results of eight HSHDC tensile specimens: (a) No. 1 to 4; and (b) No. 5 to 8.[7] (Note: 1 MPa = 145 psi.)

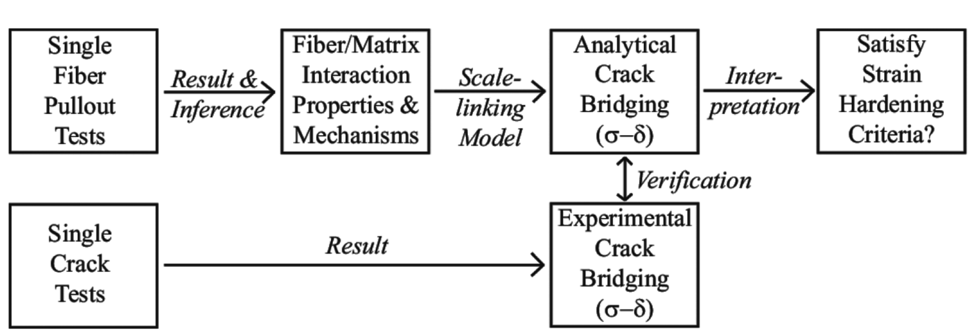

Fig. 2—Micromechanical investigation procedure.

Table 1—Mixture proportions of HSHDC

Constituent	Particle size range, μm	Mixture proportions, by weight	Weight per unit volume, kg/m^3 (lb/yd^3)
Cement (Class H)	30 to 80	1	907 (1528)
Microsilica (silica fume)	0.1 to 1	0.389	353 (595)
Ground silica (silica flour)	5 to 100	0.277	251 (423)
Silica sand	100 to 600	0.700	635 (1070)
Tap water	—	0.208; *w/cm* = 0.15	189 (318)
High-range water-reducing admixture	—	0.018	16 (27)
PE fiber*	—	0.0214	19 (33)

*Properties of PE fiber are given in Table 2.
Notes: 1 μm = 3.9 × 10^{-5} in.; *w/cm* is water-cementitious material ratio.

and 2) single-crack specimens. The details are given in the following.

Fifty single-fiber pullout specimens were prepared in this research to determine the fiber/matrix interaction properties. Thirty out of the 50 specimens contained aligned fibers (ϕ = 0 degrees). The remaining 20 specimens contained inclined fibers with five specimens for each of the four different inclination angles—ϕ = 14, 27, 37, and 45 degrees—which are equal to $\tan^{-1}(1/4)$, $\tan^{-1}(2/4)$, $\tan^{-1}(3/4)$, and $\tan^{-1}(4/4)$, respectively (Fig. 3(a)). Specimens with higher inclination angles (ϕ > 45 degrees) were not studied because their preparation resulted in breakage or folding of fibers during casting. This led to a majority of nonusable specimens and wider scatter of results than the fibers with lower inclination (common observation in SHCC[15]). Single-fiber pullout test results typically exhibit a wide scatter (even for small inclination angles and aligned fibers) and the results of individual specimens are insufficient to infer the fiber/matrix interaction properties. To overcome this inherent variability of single-fiber pullout tests, a large number (50) of specimens were tested in this research and the results from all the tests were collectively analyzed (details in following section) to compute average micromechanical properties.

The geometry of a single-fiber pullout specimen is shown in Fig. 3(b). PE and other polymer fibers are very flexible in the transverse direction and therefore cannot be simply placed in the cementitious matrix. As a result, long, uncut PE fibers were strung and tied across an opening, and the HSHDC matrix was cast around the fiber (Fig. 3(a)). Further details of the single-fiber pullout specimen preparation are given in Katz and Li.[16] After curing (procedure is given in the following), the single-fiber pullout specimens were cut at varied depths (d in Fig. 3) so as to vary the fiber embedment lengths (L_e in Fig. 3(b)) and prepared for testing at 28 days.

The setup for single-fiber pullout tests is schematically shown in Fig. 3(c). The free end of the fiber was glued between two aluminum plates, which were held by the top grip of a tensile testing system. The bottom cross section of the specimen was glued to a pedestal screwed into a high-precision load cell with a maximum capacity of 5 N (1.1 lb) and ±0.25% full-scale accuracy. The load cell was attached in series to an x-y displacement stage that was held by the bottom grips of the test system. The free length of the fiber between the plates and the matrix face was kept constant at approximately 2 mm (0.079 in.). The test was performed under displacement control at the rate of 1 μm/s (3.9 × 10^{-5} in./s). In this test, the pullout load and the displacement of the bottom grip relative to the fixed top grip were recorded. The elastic stretching of the free fiber length (2 mm [0.079 in.]) was estimated based on the in-place Young's modulus of the PE fiber (Table 2) and the pullout load. This elastic stretching was subtracted from the relative displacement u of grips to compute the pullout displacement of the PE fiber relative to the matrix face. It was assumed that slippage and stretching in the glued portion of the fiber inside the aluminum plates were negligible. Hence, the single-fiber pullout tests were conducted under quasi-static loading, and pullout load and relative displacement were recorded using appropriate sensors.

Table 2—Geometry and mechanical/physical properties of PE fiber

Fiber properties	Values
Average diameter d_f, μm (in.)	28 (0.0011)
Average length L_f, mm (in.)	12.7 (0.5)
Volume fraction V_f, %	2
Nominal strength σ_{f0}, MPa (ksi)	3000 (435)
Nominal Young's modulus, GPa (ksi)	100 (14,500)
In-place Young's modulus E_f, GPa (ksi)	30 (4350)
Elongation at break, %	3.1
Specific gravity	0.97
Melting temperature, °C (°F)	150 (302)

One length scale higher, the collective bridging behavior of multiple fibers across a crack in HSHDC was empirically determined by single-crack tests using notched rectangular coupon specimens. To deliberately enforce a single crack in a material that naturally tends to undergo multiple cracking, the specimen geometry and test setup schematically shown in Fig. 4, and modeled after Paegle and Fischer,[17] are used. For preparing such specimens, six rectangular coupons of HSHDC with dimensions of 305 x 76 x 12.7 mm (12 x 3 x 0.5 in.) were cast and cured using the procedure described in the following. After curing, a continuous notch 600 μm (0.024 in.) wide was made all around the specimen with depths of 15 mm (0.59 in.) on the lateral sides and 2 mm (0.079 in.) on the other two sides (Fig. 4, Section A-A). The notch forces the crack to occur at that section due to stress concentration and the substantially reduced cross-sectional area ensures the exhaustion of the bridging capacity at stress levels lower than that required to trigger cracks in the rest of the specimen. These specimens were tested under direct tension using a displacement-controlled closed-loop test system at the rate of 0.5 mm/min (0.02 in./min). The crack opening was computed as the average of extensions of two

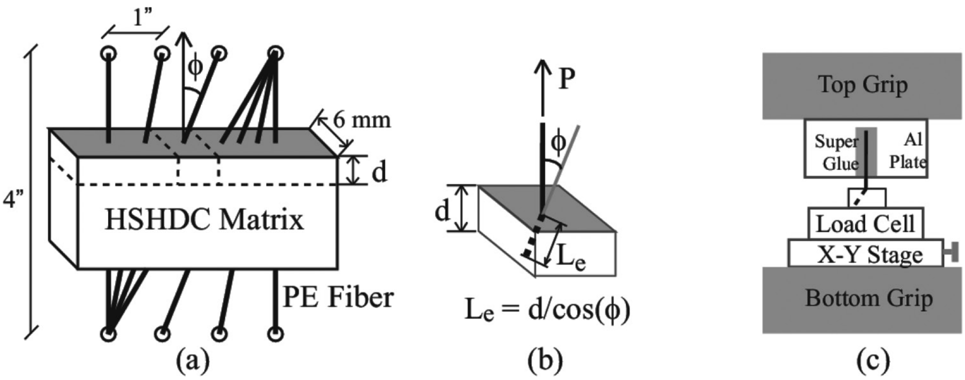

Fig. 3—Single-fiber pullout test: (a) casting of specimens; (b) one specimen; and (c) test setup. (Note: 1 in. = 25.4 mm; 1 mm = 0.039 in.)

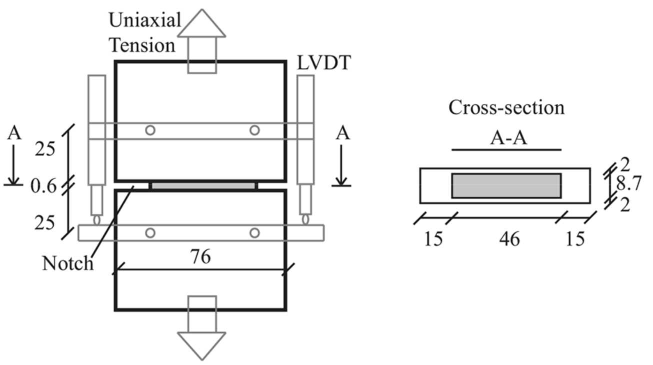

Fig. 4—Notched rectangular specimen geometry and test setup. (Note: All dimensions in mm; 1 mm = 0.039 in.)

ultra-precision linear variable displacement transducers (LVDTs) (maximum nonlinearity of ±0.25% full scale; full-scale range is 10 mm [0.4 in.]) mounted parallel to the two side edges of the coupons (Fig. 4), and the bridging stress was computed as tensile load divided by the area of the ligament (46 x 8.7 mm [1.8 x 0.34 in.]).

An elevated temperature curing procedure for accelerating the hydration process was adopted for both types of HSHDC specimens in this research. In this procedure, all specimens were demolded after 2 days of casting and kept at room temperature (23 ± 3°C [73 ± 5°F]) in water for the next 7 days. This was followed by 5 days of curing in water at 90°C (194°F) and 3 days in air at 90°C (194°F). Subsequently, the specimens were stored in air at room temperature until they were tested at 28 days after casting. The same curing procedure was adopted in the HSHDC specimens for composite properties determination in Ranade et al.[7]

EXPERIMENTAL RESULTS

Single-fiber pullout test results

While the complete set of test curves and summary of results is given in the Appendix*, for clarity of the figure and the following discussion, the test curves of five representative specimens with varying embedment lengths and inclination angles ϕ are shown in Fig. 5. It should be noted that the abscissa units in Fig. 5(a) and (b) are deliberately kept distinct. The abscissa of Fig. 5(a), intended to show the effect of varying embedment length in aligned fibers (ϕ = 0 degrees), is relative displacement u (mm), whereas the abscissa of Fig. 5(b), intended to show the effect of the varying inclination angle, is normalized relative displacement u/L_e (normalized by the respective embedment lengths). The electron micrographs of the pulled-out ends of the fiber that were embedded inside the matrix before pullout are shown in Fig. 6 (discussed in detail in the following).

Similar to a typical polymer fiber pullout of SHCC,[8-10] two distinct phases can be observed in the test curves shown in Fig. 5, which are debonding (prepeak, monotonically increasing) and pullout (postpeak/kink). The debonding process, in general, results from the breaking down of the interfacial chemical bond G_d plus the stretching of the fiber segment in the debonded zone against the fiber/matrix interfacial frictional bond, τ_0.[8] The load increases during this debonding process as additional energy is required to extend the debonding zone, until the entire embedded segment of the fiber is debonded. After complete debonding, the fiber enters the pullout phase in which the entire embedded segment of the fiber pulls out against interfacial friction only with continuously reduced embedment length. Due to linear reduction of the embedded perimeter area of the fiber with relative displacement of the fiber, u, the pullout load should also decay linearly with u. It is observed in Fig. 5, however, that the test curves in the pullout phase show slight curvatures (concave down), implying the presence of a small amount of slip hardening β,[9] which means an increase in frictional bond with slippage. The load carried by the fiber for a given embedment length is also magnified in both debond and pullout phases at non-zero inclination angles due to the snubbing effect[15] (characterized by snubbing coefficient f) between the inclined fibers and the matrix. This physical understanding of the mechanisms involved in a single-fiber pullout has been used to satisfactorily model the pullout behavior of SHCC.[10] As discussed in the following, however, the pullout phase of inclined fiber pullout of PE fibers embedded in the HSHDC matrix cannot be completely captured by these mechanisms and, as a result, a new inclination-dependent hardening mechanism is proposed for HSHDC.

Deduction of fiber/matrix interaction properties (τ_0, G_d, and β) for aligned fibers (ϕ = 0 degrees)

According to Lin et al.,[8] the load carried by the fiber during the debonding, P_{debond}, stage can be modeled using Eq. (1) in terms of relative displacement u (assuming $V_f \approx 0$ for a single fiber and, therefore, the volume weighted modulus ratio $\eta = 0$).

---

*The Appendix is available at **www.concrete.org** in PDF format as an addendum to the published paper. It is also available in hard copy from ACI headquarters for a fee equal to the cost of reproduction plus handling at the time of the request.

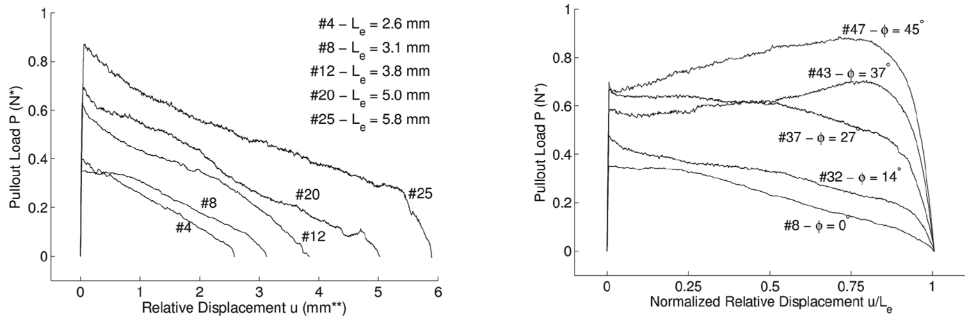

(a) Variable L_e ($\phi = 0°$) (b) Variable ϕ (L_e almost same: 3 to 4 mm)

Fig. 5—Representative single-fiber pullout curves. (Note: # denotes specimen number corresponding to Table A1; ϕ is fiber inclination angle; 1 N = 0.225 lb-ft; 1 mm = 0.039 in.)

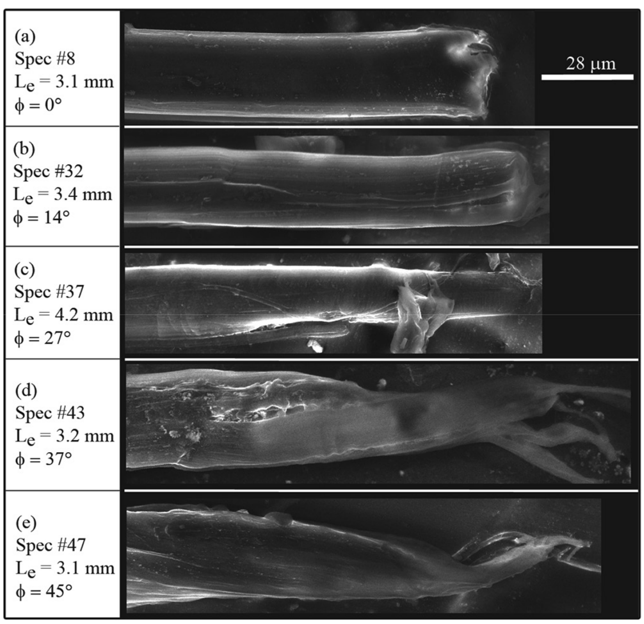

Fig. 6—SEM-generated micrographs of embedded ends of pulled-out fibers. (Note: 1 mm = 0.039 in.)

$$P_{debond} = e^{f\phi}\sqrt{\left(\tau_0 u + G_d\right)\pi^2 E_f d_f^3 / 2}$$
$$\forall u \le u_0 = \frac{2\tau_0 L_e^2}{E_f d_f} + \sqrt{\frac{8G_d L_e^2}{E_f d_f}} \tag{1}$$

where E_f and d_f are in-place Young's modulus and average diameter of the fiber (Table 2), respectively; τ_0 and G_d are fiber/matrix interfacial parameters of frictional bond and chemical bond; f is the snubbing coefficient; and u_0 is the critical relative displacement at complete debonding of the fiber and computed from fiber/matrix properties. Substituting $u = u_0$ in Eq. (1) yields the expression in Eq. (2) for peak load P_{peak} at complete debonding for aligned fibers (ϕ = 0 degrees).

$$P_{peak} = \pi d_f \tau_0 L_e + \sqrt{\pi^2 G_d E_f d_f^3 / 2} \tag{2}$$

Assuming constant G_d, Eq. (2) represents a linear relation between the variables P_{peak} and L_e. This linear relation

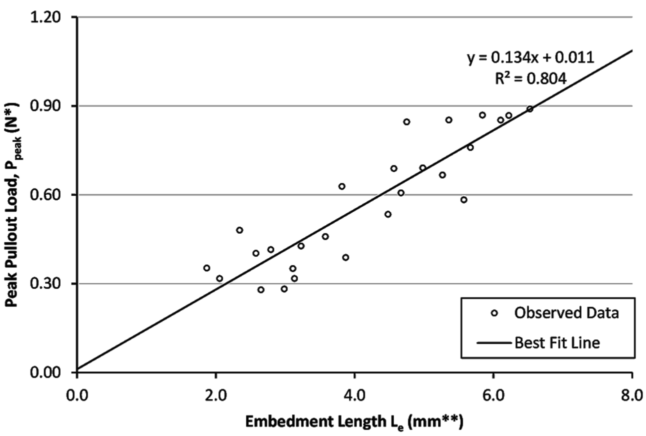

Fig. 7—Deduction of interfacial bond (τ_0 and G_d) using only aligned fiber pullout specimens. (Note: 1 N = 0.225 lb-ft; 1 mm = 0.039 in.)

assumes negligible slip-hardening during the debonding stage due to relatively small slippage compared with that during the pullout stage. Out of the 30 aligned fiber specimens (ϕ = 0 degrees [Fig. A1(a) to (d)]), four fibers ruptured before reaching the peak debond load, and are therefore excluded from the analysis (marked N/C in Table A1). The remaining 26 debond loads (P_{peak}) of aligned fiber pullout curves are summarized in Table A1 and plotted against their respective embedment lengths in Fig. 7. Using the slope (equal to 0.134) of the best-fit straight line (shown in Fig. 7) and the fiber diameter (d_f = 28 μm [0.01 in.]), the frictional bond τ_0 is computed equal to 1.52 MPa (220 psi) from Eq. (2). The chemical bond G_d is approximately equal to 0 J/m^2 (0 lb-ft/ft^2) due to a negligibly small y-intercept (0.011). The absence of chemical bond is expected with PE due to its hydrophobic nature. This is further verified by the pullout curves (Fig. 5) that show no sudden drop in load after the peak, which would otherwise correspond with the sudden release of energy accompanying the unstable propagation of the chemically debonding zone as the embedded end of the fiber is approached.

Next, the slip-hardening parameter β is determined from the postpeak curvatures of the aligned fiber pullout curves (Fig. 5(a)). The slip-hardening parameter is computed by best fitting the observed post-peak (pullout phase) inclined fiber pullout curves with the quadratic (in u) pullout load model in Eq. (3)[8] using least-square estimation with one unknown variable, β.

$$P_{pullout} = \pi d_f \tau_0 \left[1+\beta\left(u-u_0\right)\right]\left[L_e-\left(u-u_0\right)\right]e^{f\phi} \quad (3)$$
$$\forall u > u_0$$

where $P_{pullout}$ is the pullout load (post-peak ordinate in Fig. 5). The values of β thus computed for aligned fibers are summarized in the Appendix. The average slip-hardening parameter in HSHDC is 0.003, which is approximately two orders of magnitude smaller than that observed in SHCC using PVA fibers.[18] The high-performance PE fiber used in HSHDC is more abrasion-resistant than the PVA fiber in SHCC. In addition, the matrix "tunnel" surrounding the PE fiber in HSHDC is significantly smoother than SHCC due to ultra-fine filler (microsilica) and dense particle packing. Both of these factors result in small slip-hardening in HSHDC in spite of a high frictional bond.[19]

Deduction of snubbing coefficient *f* for inclined fibers (ϕ > 0 degrees)

The snubbing coefficient f is computed from the peak loads at complete debonding of the remaining 20 specimens with inclined fibers (ϕ > 0 degrees [Fig. 5(b) and A1(e) to (f)]). It was shown in a previous study[15] that the snubbing effect can be modeled as

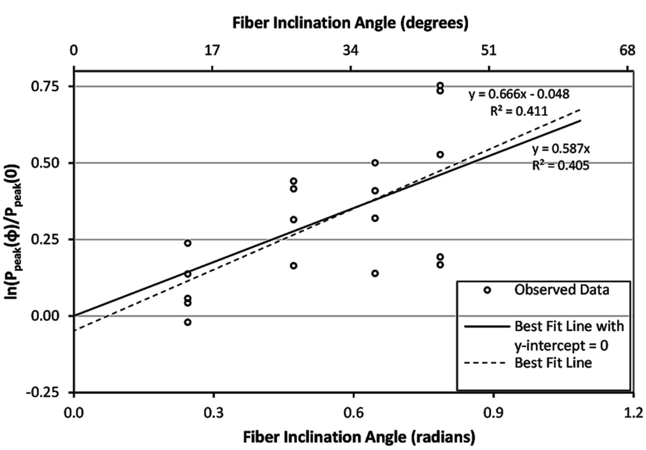

*Fig. 8—Deduction of snubbing coefficient (*f*) using only inclined fiber pullout specimens.*

$$\ln[P_{peak}(\phi)/P_{peak}(0)] = f\phi \quad (4)$$

where $P_{peak}(\phi)$ is the peak load for a specimen with fiber inclination angle of ϕ and embedment length L_e; and $P_{peak}(0)$ is the computed peak load, using Eq. (2), for an aligned fiber with the same L_e and the average τ_0 of 1.52 MPa (220 psi) determined previously. The left-hand side of Eq. (4) is plotted for 18 out of 20 inclined fiber pullout specimens against ϕ in Fig. 8 along with the best-fit straight line (dashed line). All values are also summarized in Table A1. The remaining two specimens ruptured prematurely before complete debonding and are therefore excluded from this analysis. The best-fit line (dashed line) does not pass through the origin because the average τ_0 (1.52 MPa [220 psi]) for the aligned fibers used to compute $P_{peak}(0)$ is different from the average interfacial frictional bond of the inclined fibers due to the inherent variability described previously. To fit the model in Eq. (4), another best-fit line (solid line in Fig. 8) with the y-intercept forced to zero is computed. The change in slope of the two lines is only approximately 10%. It is assumed that the fibers with inclinations higher than 45 degrees will follow a similar trend. The snubbing coefficient is thus determined equal to 0.59.

Proposed inclination-dependent hardening mechanism

The fiber/matrix interaction mechanisms described previously and the micromechanical properties deduced therefrom, although largely descriptive of HSHDC, are incomplete in fully capturing the pullout behavior of the inclined PE fibers embedded in the HSHDC matrix. Figure 9(a) shows the observed and modeled pullout behavior of a randomly chosen, representative inclined fiber pullout specimen (number 43 in Table A1 with ϕ = 37 degrees). The computed curve using the SHCC model (Eq. (1) and (3)) in Fig. 9(a) does not correspond with the observed behavior in the post-peak pullout phase (assuming the fiber/matrix interaction properties obtained for aligned fibers are the same for inclined fibers). Figure 9(b) shows the difference between the observed and the (SHCC) modeled load plotted against the post-debonding (post-peak) relative displacement ($u - u_0$). As the difference in load seems to increase linearly with ($u - u_0$), a best-fit straight line closely fitting 90% of the curve is plotted in Fig. 9(b) with a slope ($\mu\cdot\phi$) equal to 0.239 N/mm

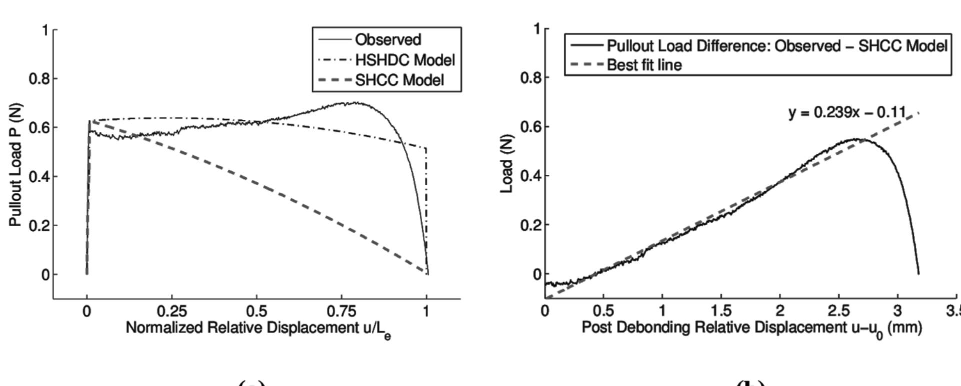

Fig. 9—(a) Observed and modeled single-fiber pullout behavior of Specimen 43; and (b) deduction of $\mu\cdot\phi$ for Specimen 43. (Note: 1 N = 0.225 lb-ft; 1 mm = 0.039 in.)

(239 N/m). Following the same procedure, such slopes ($\mu \cdot \phi$) are obtained for all the inclined fiber pullout specimens and plotted in Fig. 10 (all values are summarized in Table A1) against the fiber inclination angles. A straight line best fitting these data points and passing through the origin is further drawn to determine the inclination hardening parameter (constant for the composite) μ equal to 386 N/(m-rad) (26.4 lb/(ft-rad)), which is defined as the increase in pullout load per unit increase in inclination angle and slippage.

It is assumed in the analytical investigation that follows that the trend of increasing pullout load with ϕ will continue for fiber inclinations greater than 45 degrees (up to 90 degrees) as the matrix wedge sharpness increases proportionally with ϕ. However, there may be a limiting ϕ beyond which the matrix microspalling (discussed in the following) occurs due to high stress concentration at a sharp matrix wedge, which may lead to a decrease in pullout load at very large ϕ. Further tests at higher inclination angles are required to investigate this possibility; however, for the planar HSHDC specimens used in this study, the number of fibers with very high inclination angles is low (discussed in the following) and, therefore, the assumption of increasing pullout load with ϕ is largely valid for this analysis.

The pullout phase load in SHCC model (Eq. (3)) can be modified to account for μ, as shown in Eq. (5). The pullout behavior of Specimen 43 computed using HSHDC model (with μ = 386 N/(m-rad)) is plotted in Fig. 9(a), which satisfactorily fits the observed curve.

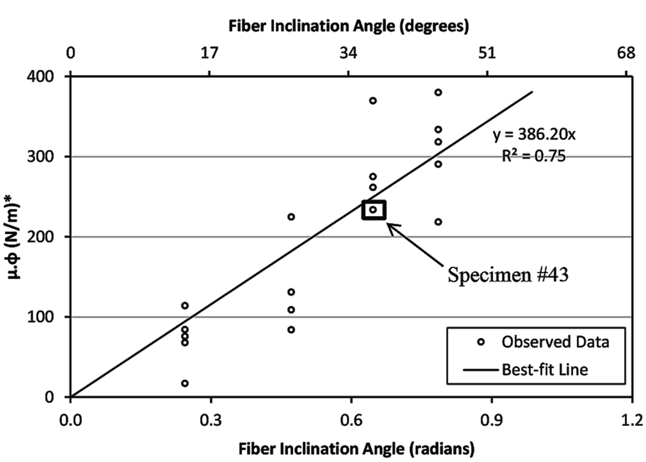

Fig. 10—Deduction of inclination hardening parameter μ. (Note: 1 N/m = 0.0685 lb/ft.)

$$P_{pullout} = \pi d_f \tau_0 [1 + \beta(u - u_0)][L_e - (u - u_0)]e^{f\phi} + \mu\phi(u - u_0) \quad \forall u > u_0 \tag{5}$$

A plausible physical explanation for the inclination-dependent hardening mechanism follows. Due to the increase in tip sharpness of the matrix wedge (Fig. 11(a)) with an increase in fiber inclination angle, there is an increase in the clamping effect at the wedge tip as it digs into the fiber in the transverse direction (depicted exaggeratedly in Fig. 11(b)). This clamping force also increases with an increase in slip ($u - u_0$) because of the degradation of the fiber cross section and resulting blockage of the fiber exit point. As a result, the cross section of the embedded fiber segment slowly reduces, causing a pencil-tip shape along the length of the fiber (Fig. 11(c)). This explanation is supported by the electron micrographs (Fig. 6), displaying the pulled-out ends of representative fibers that had been embedded in the matrix at each of the inclinations used in this study. These micrographs were obtained using a scanning electron microscope (SEM). The micrographs clearly show that the degradation of the fiber increases (in spite of similar embedment lengths) with inclination angle and slip, which supports the mathematical formulation (Eq. (5)) and the aforementioned physical explanation.

This mechanism is in contrast with the microspalling phenomenon[20] (Fig. 11(d)) observed in polymer fiber pullout in the moderate-strength SHCC matrix. In SHCC, the fiber is stronger than the matrix wedge tip and spalls the matrix, causing a slight softening of the pullout load curve, whereas in HSHDC, the very-high-strength matrix (almost twice the fracture toughness as SHCC) resists the spalling and, instead, clamps the fiber, causing hardening of the pullout load curve.

Single-crack test results

The bridging stress (σ)-crack opening (δ) relation (σ-δ curve) of HSHDC was empirically determined from six single-crack tests with notched rectangular coupons (Fig. 4) tested under direct tension. All the six measured curves are shown in Fig. 12, along with the computed curves (shown by dashed lines) based on an analytical model detailed in the next section. Two distinct phases are observed in the measured curves. Initially, when the ligament is uncracked, the tensile load rises elastically with applied displacement as the cementitious matrix carries the majority of the load. This is accompanied by a proportional increase in stress inten-

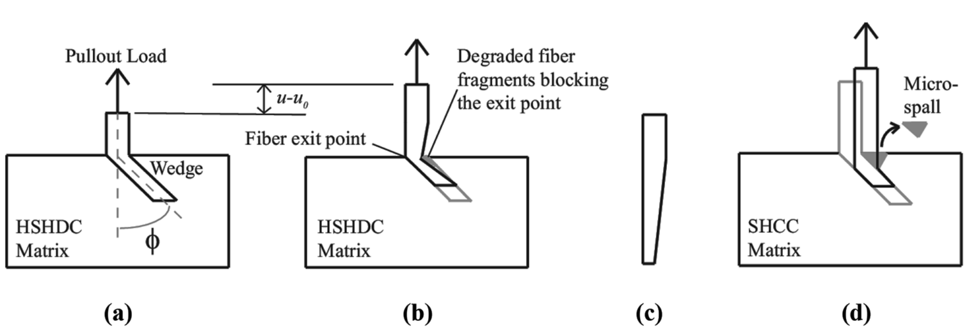

Fig. 11—Schematic depiction of inclination-dependent hardening mechanism: (a) HSHDC matrix wedge at u = u_0; (b) fiber degradation at u > u_0; (c) pencil-tip-shaped pulled-out fiber end; and (d) microspall phenomenon observed in SHCC.[20]

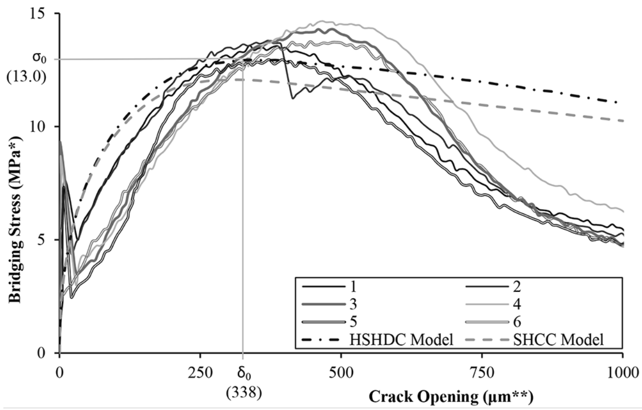

Fig. 12—Measured and computed (using SHCC and HSHDC models) crack-bridging relation of HSHDC rectangular coupons. (Note: 1 MPa = 145 psi; 1 μm = 3.9 × 10^{-5} in.)

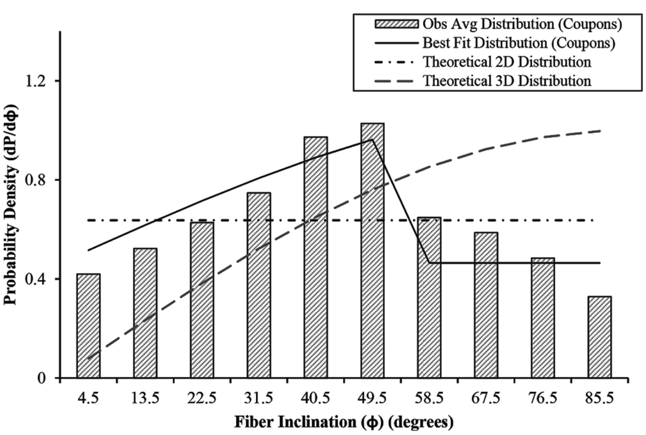

Fig. 13—Observed and best-fit fiber inclination distributions.

sity at the notch tip. Once the stress intensity exceeds the fracture toughness of the matrix, sudden crack propagation occurs, resulting in loss of tensile stress previously carried by the matrix (Fig. 12). After this point, applied tensile load is in equilibrium with bridging stress σ transferred by the fibers across the crack. The tensile load increases again with increasing crack opening δ until the collective bridging capacity of the fibers is exhausted. The bridging stress gradually decreases after this point as an increasing number of fibers are either pulled out or broken. For the multiple cracking criteria discussed in the following, only the portion of the σ-δ curve up to the bridging capacity is relevant. The average bridging capacity (peak of σ-δ curve) thus measured at the notched sections of the six specimens is 13.8 MPa (2.0 ksi).

ANALYTICAL INVESTIGATION

The objective of this analytical investigation is to predict the σ-δ relation of HSHDC using a statistical scale-linking model (Eq. (6)).[12] The deduced fiber/matrix interaction properties described in previous sections are used as inputs in this model.

$$\sigma(\delta) = \frac{V_f}{A_f}\int_0^{\pi/2}\int_0^{(L_f/2)\cos(\phi)} P(u)p(z)p(\phi)dzd\phi \qquad (6)$$

where δ is the crack opening equal to the sum of fiber pullout relative displacements (u_1 and u_2) on both sides of the crack (compatibility). $P(u)$ is the single-fiber pullout load modeled by Eq. (1) and (5). By enforcing the equilibrium condition $P(u_1) = P(u_2)$, u_1 and u_2 are determined, as detailed in Yang et al.[20] L_e is the shorter of the two embedment lengths on either side of the crack. $p(z)$ is the distribution of embedded fiber's centroidal distance from the crack plane (assumed to be $2/L_f$).[12] The probability density function $p(\phi)$ mathematically describes the fiber inclination distribution in HSHDC coupon specimens (which were used in the aforementioned single-crack tests) determined as explained as follows.

The fiber inclination distribution $p(\phi)$ was experimentally determined (Fig. 13) using fluorescence microscopy employing the method described in Lee et al.[21] The specimen preparation and analysis procedures are described in Ranade et al.[22] Best-fit continuous functions for the observed inclination distribution in HSHDC coupons are given by Eq. (7) and plotted (as a solid line) in Fig. 13 along with the typically assumed theoretical two-dimensional (2-D) ($p(\phi) = 2/\pi$) and three-dimensional (3-D) ($p(\phi) = \sin(\phi)$) uniformly random distributions. The best-fit distribution in HSHDC coupons is modeled as a linear combination of the 2-D and 3-D uniformly random distributions. The reason for restricting the 3-D distribution at 54 degrees is the observation of distinct drop in histogram after the class interval of 45 to 54 degrees (with the class mark of 49.5 degrees), which may be caused by the limited thickness (12.7 mm [0.5 in.]) of coupons. The weights for 2-D and 3-D distributions are determined using least-square estimation in one variable, w, to best fit the observed distribution. The best-fit value of w is 0.73 for HSHDC coupons.

$$\begin{aligned} p(\phi) &= w(2/\pi) + (1-w)\sin(\phi)/[\cos(0°) - \cos(54°)] \quad && \forall\phi \in [0°, 54°] \\ p(\phi) &= w(2/\pi) && \forall\phi \in (54°, 90°] \end{aligned} \qquad (7)$$

Equation (6) is numerically computed to yield the σ-δ relation (for $V_f = 2\%$) of HSHDC coupon specimens using both the HSHDC model (incorporating inclination-dependent hardening) and the SHCC model. Both the modeled curves are plotted (dashed lines) in Fig. 12 along with experimentally determined σ-δ relations using single-crack tests. The σ-δ curve computed using the HSHDC model fits the observed curves more closely than the curve computed using the SHCC model, which further supports the aforementioned inclination-dependent hardening mechanism unique to HSHDC. The bridging capacity σ_0 (at δ_0 = 338 μm) of the computed curve is 13.0 MPa (1.9 ksi) for the HSHDC model and 12.0 MPa (1.7 ksi) for the SHCC model.

The computed curve using HSHDC model is initially steeper than the experimental curves. This behavior has been previously explained by Cook-Gordon effect,[20] in which premature fiber/matrix interface debonding results in wider crack opening. The Cook-Gordon effect is not included in the computed σ-δ curves. In spite of higher initial slope of the computed σ-δ curve, it achieves a bridging capacity [13.0 MPa (1.9 ksi)] similar to experimental curves as it is governed by the strength and geometry of the fibers, interfacial bond, and hardening properties. The higher slope of the computed σ-δ curve results in a conservative estimate of the complimentary energy (discussed in the following), which is desirable for checking the energy criterion of steady-state crack propagation. The softening branch (post-peak) of the computed curve overshoots the observed bridging stress. This may be caused by the frictional pullout load decay with additional slippage caused by the Cook-Gordon effect in the softening phase.[23] Overall, the computed σ-δ curve of HSHDC shows a good agreement with the experimental curves and is a useful tool for evaluating strain hardening criteria, as discussed in the following.

DISCUSSION OF RESULTS

Detailed comments and discussion of experimental results have been included in the previous sections. In this section, the analytically computed σ-δ relation of HSHDC is discussed in light of the two necessary micromechanics-based conditions for multiple cracking to establish a micromechanics basis for the high tensile ductility of HSHDC (Fig. 1) reported in Ranade et al.[7] The two conditions are the strength criterion and the energy criterion.[24]

The strength criterion (Eq. (8)) to form more than one crack requires that the crack initiation stress ($\sigma_{ci(fc)}$) for the first crack is lower than the minimum bridging capacity, $\min(\sigma_0)$.[24] Stronger inequality implies that more margin is available to trigger multiple cracks.

$$\sigma_{ci(fc)} \leq \min(\sigma_0) \tag{8}$$

The variable σ_{ci} varies in an HSHDC specimen from one defect to another due to the difference in defect sizes caused by trapped air voids, interfacial weakness, and other reasons. The first crack is typically formed at the largest defect site at stress $\sigma_{ci(fc)}$, which is reported in a companion paper[7] as 8.4 MPa (1.2 ksi). The variable σ_0 (Fig. 12) also varies in a specimen due to a varying number of fibers at each cross section caused by inhomogeneous distribution of fibers in the matrix. Among all the cracks formed, the weakest bridged crack is typically the one with the least number of effective bridging fibers (least fiber-volume fraction V_f). Through fluorescence microscopy and statistical analysis (Fig. A2 in the Appendix), it was determined that more than 97% of the HSHDC sections (two standard deviations more than the average) have an effective volume fraction of 1.7% or higher. The $\min(\sigma_0)$ can therefore be computed to be equal to 11.0 MPa (1.6 ksi) using the computed σ_0 of 13.0 MPa (1.9 ksi) for $V_f = 2\%$ (13 MPa × 1.7/2 = 11 MPa). Hence, $\min(\sigma_0)/\sigma_{ci(fc)}$ for HSHDC is equal to 1.3, which not only satisfies the strength criterion in Eq. (8) but also represents a stronger inequality of $\min(\sigma_0)/\sigma_{ci(fc)} > 1.2$ required for robust multiple cracking.[24]

The second criterion for multiple cracking is the energy criterion represented by Eq. (9).

$$\frac{K_m^2}{E_m} = G_m \approx J_{tip} \leq J_b' = \sigma_0\delta_0 - \int_0^{\delta_0} \sigma(\delta)d\delta \tag{9}$$

It is based on the path-independent J-integral formulation of the steady-state crack propagation problem in composites.[25] In essence, the energy criterion requires that the total available crack-driving energy J_b' should be greater than the composite's resistance to crack propagation, J_{tip}. The available crack-driving energy (also known as complementary energy J_b') can be interpreted as elastic strain energy released during steady-state crack propagation (σ_0 times δ_0 [Fig. 12]) less that absorbed by the bridging fibers (the integral term in Eq. (9)) near the crack tip as the crack opens up to the value of δ_0.[13] J_{tip} can be approximated to G_m (fracture energy of the matrix) in the case of brittle matrix composites such as HSHDC and SHCC with low fiber volumes (2%). G_m can be estimated in terms of matrix fracture toughness K_m and matrix modulus E_m as K_m^2/E_m. K_m for the HSHDC matrix is 1.1 MPa√m (1.0 ksi√in.), experimentally determined using notched beam specimens following the ASTM E399[26] procedure. E_m is assumed equal to the composite tensile modulus E_c, as the fiber-volume fraction is very small (2%). In Ranade et al.,[7] E_c is reported equal to 48.4 GPa (7018 ksi). Thus, G_m is computed equal to 25 J/m^2 (0.14 psi-in.). Complementary energy J_b', corresponding to $V_f = 1.7\%$ (J_b' increases with V_f for HSHDC), is numerically computed equal to 682 J/m^2 (3.9 psi-in.) by subtracting the area under the σ-δ curve from the product of $\sigma_0\delta_0$. Therefore, J_b'/J_{tip} is 27, which comfortably satisfies the energy criterion of Eq. (9) and the more stringent requirement of $J_b'/J_{tip} > 3$ for robust multiple cracking.[24]

The properties of $\min(\sigma_0)$ and J_b' are computed previously for a rectangular coupon specimen of HSHDC, which can vary depending on the fiber distributions (Fig. 13). For theoretical 2-D distribution and $V_f = 1.7\%$ (assuming similar variability as coupon specimens), the $\min(\sigma_0)$ and J_b' computed for HSHDC are 10.2 MPa (1.5 ksi) and 581 J/m^2 (3.3 psi-in.), respectively, and that for theoretical 3-D distribution are 9.4 MPa (1.3 ksi) and 468 J/m^2 (2.7 psi-in.), respectively. Both the necessary conditions of multiple cracking are satisfied in HSHDC when either of the two theoretical distributions is used for computations.

SUMMARY AND CONCLUSIONS

In this study, a detailed micromechanics-based analysis of HSHDC was performed to determine the microscale fiber/matrix interaction properties and mechanisms, which explain the experimentally observed macroscopic composite tensile ductility (3.4% tensile strain capacity) of this material in spite of its very high compressive strength (166 MPa [24.1 ksi]). The following conclusions can be drawn.

- The experimentally determined average interfacial frictional bond τ_0 between the PE fiber and HSHDC matrix is 1.52 MPa (220 psi). Such high interfacial frictional bond facilitated by dense particle packing of the very-high-strength matrix, accompanied by a negligible chemical bond G_d, results in a high complementary energy J_b', favorable for macroscopic strain-hardening response of HSHDC under direct tension. For comparison, the measured τ_0 for the same fiber in a moderate-strength matrix has been reported to be 0.54 to 0.76 MPa (78 to 110 psi).[27] Other fiber/matrix interaction properties of HSHDC determined in this research are snubbing coefficient ($f = 0.59$) and slip-hardening parameter ($\beta = 0.003$). All micromechanical properties show wide scatter due to material inhomogeneity (similar to SHCC) at the microlength scale.
- A new inclination-dependent hardening mechanism of fiber pullout in HSHDC is proposed, as the existing fiber/matrix interaction mechanisms developed for SHCC are insufficient in completely describing the experimentally observed inclined fiber-pullout behavior of PE fibers embedded in a very-high-strength HSHDC matrix. The SHCC micromechanical model in the pullout phase is modified to incorporate this mechanism. The SEM micrographs provide evidence for this mechanism and its mathematical formulation. The closer match of the experimental curves to the computed σ-δ relation obtained using the modified HSHDC pullout

model when compared with that from the SHCC model provides further support to this mechanism. The newly defined inclination hardening parameter μ (constant property of the composite) is 386 N/(m-rad) (26.4 lb/(ft-rad)) for HSHDC.

- The min(σ_0) (11.0 MPa [1.6 ksi]) and J_b' (682 J/m^2 [3.9 psi-in.]) determined for HSHDC satisfy the necessary conditions for robust multiple cracking, thus providing a rational basis for the observed composite tensile ductility of HSHDC. It is further concluded that in spite of a higher matrix toughness compared with SHCC, HSHDC maintains tensile ductility by enhanced fiber bridging with a strong interfacial frictional bond and fiber strength.

ACKNOWLEDGMENTS

This research at the University of Michigan was supported by a research contract (W912HZ-08-C-0056) from the U.S. Army Engineer Research and Development Center (ERDC), Vicksburg, MS. Helpful discussions with T. Slawson (ERDC) and T. Cummins (ERDC) are gratefully acknowledged. The material suppliers: Honeywell, Lafarge, Elkem, US Silica, and WR Grace are duly acknowledged for providing the materials used in this research. Permission to publish was granted by Director, Geotechnical and Structures Laboratory at ERDC.

REFERENCES

1. Neeley, B. D., and Walley, D. M., "Very High-Strength Concrete," *The Military Engineer*, V. 87, No. 572, 1995, pp. 36-37.

2. Richard, P., and Cheyrezy, M., "Reactive Powder Concretes with High Ductility and 200-800 MPa Compressive Strength," *Concrete Technology: Past, Present, and Future*, SP-144, P. K. Mehta, ed., American Concrete Institute, Farmington Hills, MI, 1994, pp. 507-518.

3. Li, V. C., "On Engineered Cementitious Composites (ECC)—A Review of the Material and Its Applications," *JCI Journal of Advanced Concrete Technology*, V. 1, No. 3, 2003, pp. 215-230.

4. Fukuyama, H.; Matsuzaki, Y.; Nakano, K.; and Sato, Y., "Structural Performance of Beam Elements with PVA-ECC," *Proceedings of HPFRCC 3*, H. W. Reinhardt and A. Naaman, eds., Mainz, Germany, 1999, pp. 531-542.

5. RILEM, "Durability of Strain-Hardening Fibre-Reinforced Cement-Based Composites (SHCC)," F. Wittman and G. Van Zijl, eds., *RILEM State-of-the-art Report*, V. 4, 2011, pp. 9-39.

6. RILEM TC 208-HFC, "Strain Hardening Cement Composites: Structural Design and Performance," K. Rokugo and T. Kanda, eds., *RILEM State-of-the-art Report*, V. 6, 2013, pp. 3-49.

7. Ranade, R.; Li, V. C.; Stults, M. D.; Heard, W. F.; and Rushing, T. S., "Composite Properties of High-Strength, High-Ductility Concrete," *ACI Materials Journal*, V. 110, No. 4, July-Aug. 2013, pp. 413-422.

8. Lin, Z.; Kanda, T.; and Li, V. C., "On Interface Property Characterization and Performance of Fiber Reinforced Cementitious Composites," *RILEM Journal of Concrete Science and Engineering*, V. 1, 1999, pp. 173-184.

9. Li, V. C.; Wang, S.; and Wu, C., "Tensile Strain-Hardening Behavior of PVA-ECC," *ACI Materials Journal*, V. 98, No. 6, Nov.-Dec. 2001, pp. 483-492.

10. Li, V. C.; Wu, C.; Wang, S.; Ogawa, A.; and Saito, T., "Interface Tailoring for Strain-Hardening PVA-ECC," *ACI Materials Journal*, V. 99, No. 5, Sept.-Oct. 2002, pp. 463-472.

11. O'Neil, E. F., "On Engineering the Microstructure of HPC to Improve Strength, Rheology, and Frangibility," PhD dissertation, Northwestern University, Evanston, IL, 2008, p. 94.

12. Li, V. C.; Wang, Y.; and Backer, S., "A Micromechanical Model of Tension-Softening and Bridging Toughening of Short Random Fiber Reinforced Brittle Matrix Composites," *Journal of the Mechanics and Physics of Solids*, V. 39, No. 5, 1991, pp. 607-625.

13. Li, V. C., "From Micromechanics to Structural Engineering—The Design of Cementitious Composites for Civil Engineering," *JSCE Journal of Structural Mechanics and Earthquake Engineering*, V. 10, No. 2, 1993, pp. 37-48.

14. Ranade, R.; Stults, M. D.; Li, V. C.; Rushing, T. S.; Roth, J.; and Heard, W. F., "Development of High Strength High Ductility Concrete," *Proceedings of SHCC-2*, R. D. T. Filho, F. A. Silva, E. A. B. Koenders, and E. M. R. Fairbairn, eds., Rio de Janeiro, Brazil, 2011, pp. 1-8

15. Li, V. C.; Wang, Y.; and Backer, S., "Effect of Inclining Angle, Bundling and Surface Treatment on Synthetic Fibre Pullout from Cement Matrix," *Composites Journal*, V. 20, No. 2, 1990, pp. 132-140.

16. Katz, A., and Li, V. C., "A Special Technique for Determining the Bond Strength of Carbon Fibers in Cement Matrix by Pullout Test," *Journal of Materials Science Letters*, V. 15, 1996, pp. 1821-1823.

17. Paegle, I., and Fischer, G., "Evaluation of Standardized Test Methods to Characterize Fiber Reinforced Cement Composites," *Proceedings of SHCC-2*, R. D. T. Filho, F. A. Silva, E. A. B. Koenders, and E. M. R. Fairbairn, eds., Rio de Janeiro, Brazil, 2011, pp. 9-16.

18. Wang, S., and Li, V. C., "Engineered Cementitious Composites with High-Volume Fly Ash," *ACI Materials Journal*, V. 104, No. 3, May-June 2007, pp. 233-241.

19. Wang, Y.; Li, V. C.; and Backer, S., "Modeling of Fiber Pull-Out from a Cement Matrix," *Journal of Cement Composites and Lightweight Concrete*, V. 10, No. 3, 1988, pp. 143-149.

20. Yang, E. H.; Wang, S.; Yang, Y.; and Li, V. C., "Fiber-Bridging Constitutive Law of Engineered Cementitious Composites," *JCI Journal of Advanced Concrete Technology*, V. 6, No. 1, 2008, pp. 1-13.

21. Lee, B. Y.; Kim, J. K.; Kim, J. S.; and Kim, Y. Y., "Quantitative Evaluation Technique of Polyvinyl Alcohol (PVA) Fiber Dispersion in Engineered Cementitious Composites," *Cement and Concrete Composites*, V. 31, No. 6, 2009, pp. 408-417.

22. Ranade, R.; Stults, M. D.; Lee, B. Y.; and Li, V. C., "Effects of Fiber Dispersion and Flaw Size Distribution on the Composite Properties of PVA-ECC," *Proceedings of RILEM HPRCC-6*, Ann Arbor, MI, 2011, pp. 106-113.

23. Li, V. C.; Stang, H.; and Krenchel, H., "Micromechanics of Crack Bridging in Fibre Reinforced Concrete," *Materials and Structures*, No. 26, 1993, pp. 486-494.

24. Kanda, T., and Li, V. C., "Multiple Cracking Sequence and Saturation in Fiber Reinforced Cementitious Composites," *JCI Concrete Research and Technology*, V. 9, No. 2, 1998, pp. 19-33.

25. Marshall, D., and Cox, B. N., "A J-Integral Method for Calculating Steady-State Matrix Cracking Stress in Composites," *Mechanics of Materials*, V. 7, 1988, pp. 127-133.

26. ASTM E399-03, "Test Method for Plane-Strain Fracture Toughness of Metallic Materials," ASTM International, West Conshohocken, PA, 2003, 33 pp.

27. Li, V. C., and Maalej, M., "Effect of Plasma Treatment of Polyethylene Fibers on Interface and Cementitious Composite Properties," *Journal of the American Ceramic Society*, V. 79, No. 1, 1996, pp. 74-78.

APPENDIX

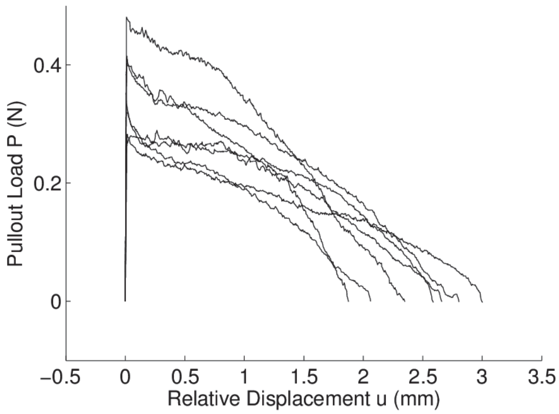

(a) $\phi = 0°$; L_e = 1.8 to 3 mm

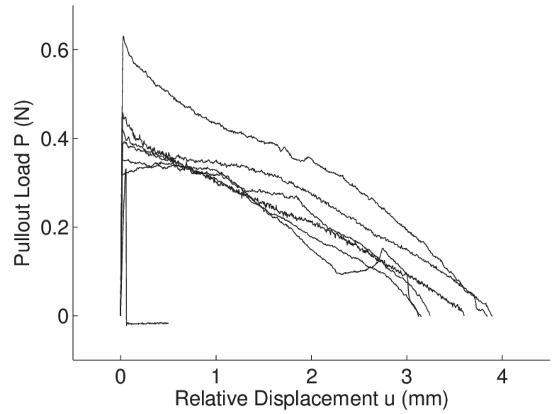

(b) $\phi = 0°$; L_e = 3 to 4 mm

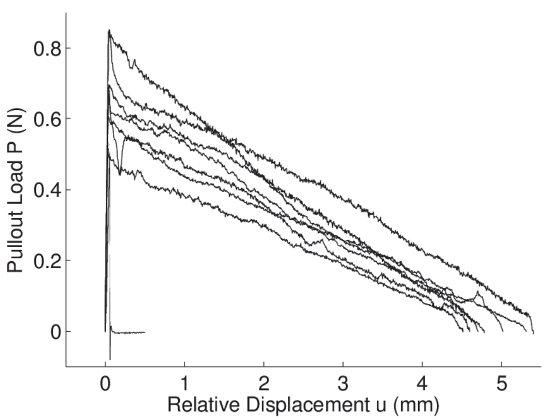

(c) $\phi = 0°$; L_e = 4 to 5.5 mm

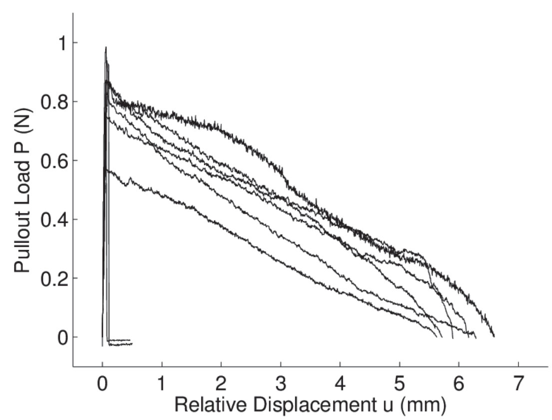

(d) $\phi = 0°$; L_e = 5.5 to 7 mm

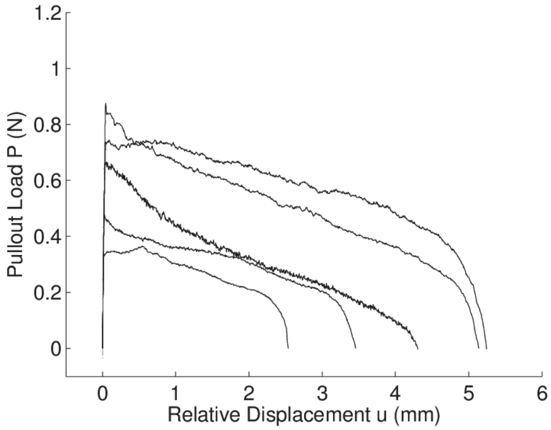

(e) $\phi = 14°$

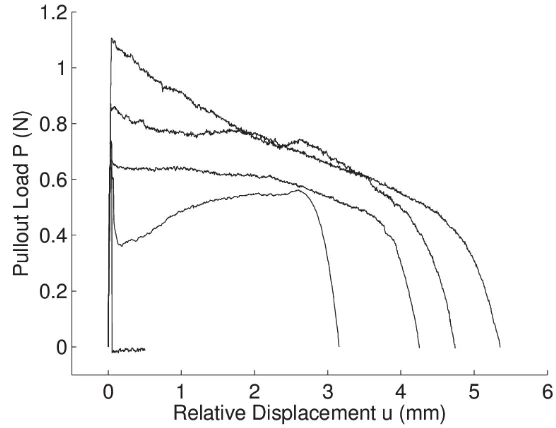

(f) $\phi = 27°$

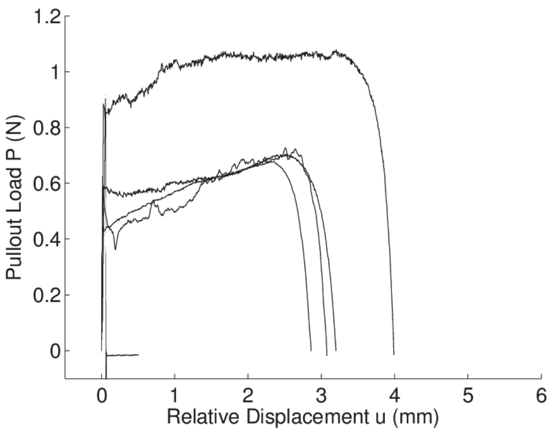

(g) $\phi = 37°$

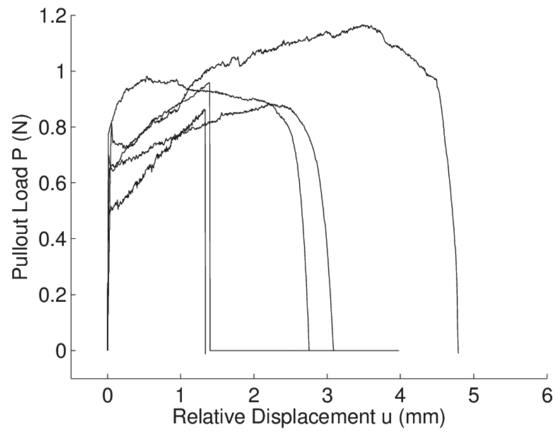

(h) $\phi = 45°$

Fig. A1–Complete single fiber pullout test curves for various fiber inclination angles (ϕ) and embedment lengths (L_e)

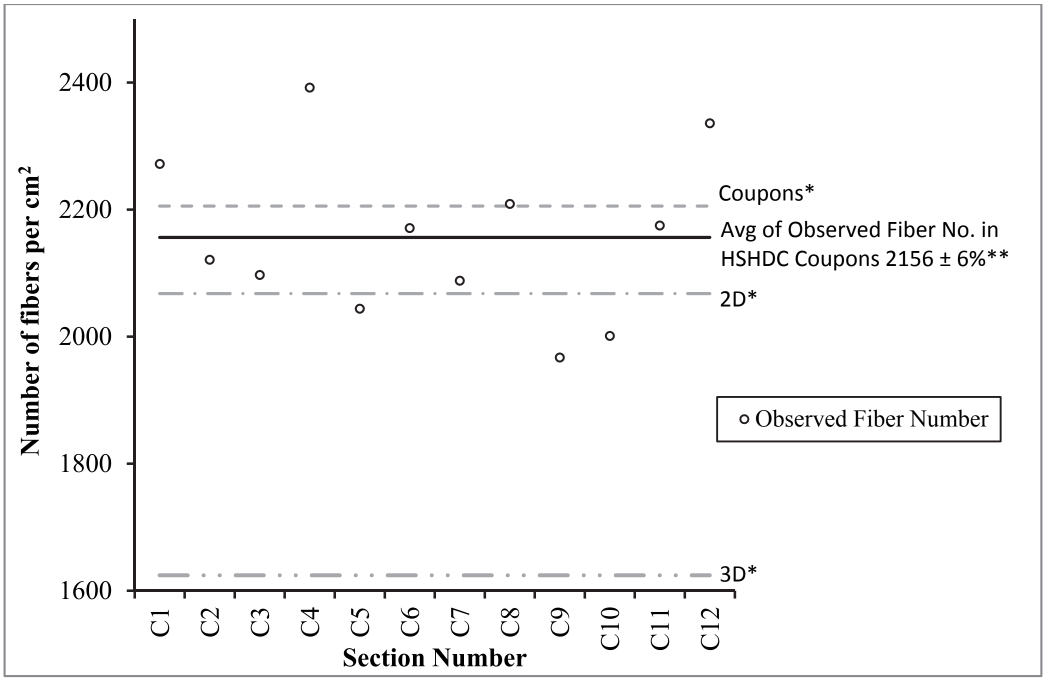

Fig. A2–Fiber number in HSHDC for various inclination distributions

* The horizontal lines corresponding to "Coupons", "2D", and "3D" distributions are computed using theoretical formula of $\eta_f V_f/A_f$ where V_f = 2%, A_f is the fiber cross-sectional area, and bridging efficiency, $\eta_f = \int_0^{\pi/2}\int_0^{(L_f/2)\cos(\phi)} p(z)p(\phi)dzd\phi$

** The standard deviation (SD) of 6.0% (of mean) is modified to 7.0% to account for the limited number of observations (12) in accordance with the statistical theory (using modification factor of 1.16); thus, 2.SD = 14%. However, the observed average of 2156 fibers/cm^2 is 97% of the computed average of 2205 fibers/cm^2 [assuming observed p(ϕ) and V_f = 2%]. Thus, min(V_f) = [(1-0.14)(2156)/2205].2% = 1.7%.

Table A1–Summary of single-fiber pullout test results

Fig. A1 Number	Specimen Number	Embedment Length (L_e) mm	Inclination Angle (ϕ) deg	Peak Debond Load (P_{peak}) N	Slip Hardening Parameter (β)	$\ln \frac{P_{peak}(\phi)}{P_{peak}(0)}$ *1	$\mu.\phi$*2 N/m
(a)	1	1.9	0	0.35	0.0305	Not applicable for $\phi = 0°$	Not applicable for $\phi = 0°$
	2	2.1	0	0.32	0.0087		
	3	2.3	0	0.48	0.0242		
	4	2.6	0	0.40	0.0063		
	5	2.6	0	0.28	0.0041		
	6	2.8	0	0.41	0.0059		
	7	3.0	0	0.28	-0.0049		
(b)	8	3.1	0	0.35	0.0023		
	9	3.1	0	0.32	0.0013		
	10	3.2	0	0.43	0.0035		
	11	3.6	0	0.46	-0.0016		
	12	3.8	0	0.63	0.0055		
	13	3.9	0	0.39	-0.0003		
	14	3.9	0	0.34	N/C*3		
(c)	15	4.5	0	0.53	-0.0023		
	16	4.6	0	0.69	-0.0003		
	17	4.7	0	0.61	-0.0001		
	18	4.8	0	0.85	0.0029		
	19	4.8	0	0.54	N/C		
	20	5.0	0	0.69	0.0002		
	21	5.3	0	0.67	-0.0021		
	22	5.4	0	0.85	0.0012		
(d)	23	5.6	0	0.58	-0.0032		
	24	5.7	0	0.76	0.0018		
	25	5.8	0	0.87	0.0025		
	26	6.1	0	0.85	-0.0020		
	27	6.2	0	1.00	N/C		
	28	6.2	0	0.87	0.0007		
	29	6.5	0	0.89	0.0013		
	30	7.0	0	0.94	N/C		
(e)	31	2.5	14	0.33	Assumed same as the average value for aligned fibers	-0.02	76
	32	3.4	14	0.49		0.06	84
	33	4.3	14	0.66		0.14	17
	34	5.1	14	0.87		0.24	68
	35	5.2	14	0.73		0.04	114
(f)	36	3.1	27	0.64		0.42	225
	37	4.2	27	0.67		0.16	131
	38	4.7	27	0.87		0.31	109
	39	5.1	27	N/C		N/C	N/C
	40	5.3	27	1.11		0.44	84
(g)	41	2.8	37	0.44		0.14	262
	42	3.1	37	0.62		0.41	275
	43	3.2	37	0.59		0.32	239
	44	4.0	37	0.88		0.50	370
	45	4.4	37	N/C		N/C	N/C
(h)	46	2.7	45	0.77		0.74	334
	47	3.1	45	0.70		0.53	291
	48	2.8	45	0.80		0.75	380
	49	4.0	45	0.63		0.17	318
	50	5.5	45	0.90		0.19	219

*1 $P_{peak}(0)$ is the theoretical peak debond load of an aligned fiber ($\phi = 0°$) of the same embedment length as the inclined fiber assuming $\tau_0 = 1.53$ MPa.

*2 $\mu.\phi$ is the product of the inclination hardening parameter μ and inclination angle ϕ (radians).

*3 N/C means "Not Computable" because of premature fiber breakage before complete debonding.